Vis Comput (2011) 27: 373–386
DOI 10.1007/s00371-011-0544-4

ORIGINAL ARTICLE

# Homotopy-based surface reconstruction with application to acoustic signals

**Ojaswa Sharma · François Anton**

Published online: 21 January 2011


**Abstract** This work introduces a new algorithm for surface reconstruction in $\mathbb{R}^3$ from spatially arranged one-dimensional cross sections embedded in $\mathbb{R}^3$. This is generally the case with acoustic signals that pierce an object non-destructively. Continuous deformations (homotopies) that smoothly reconstruct information between any pair of successive cross sections are derived. The zero level set of the resulting homotopy field generates the desired surface. Four types of homotopies are suggested that are well suited to generate a smooth surface. We also provide derivation of necessary higher order homotopies that can generate a $C^2$ surface. An algorithm to generate surface from acoustic sonar signals is presented with results. Reconstruction accuracies of the homotopies are compared by means of simulations performed on basic geometric primitives.

**Keywords** Homotopy · Continuous deformations · Surface reconstruction · Shape preserving · Acoustic signal · Sonar

## 1 Introduction

Surface reconstruction is a frequently encountered problem in computer graphics and computer vision. The reconstruction problem that we address in this paper is the one of generating a topologically and geometrically convincing surface from a set of acoustic signals acquired using multibeam echo-sounders.

O. Sharma (✉) · F. Anton
Department of Informatics and Mathematical Modeling,
Technical University of Denmark, Lyngby 2800, Denmark
e-mail: os@imm.dtu.dk

F. Anton
e-mail: fa@imm.dtu.dk

The problem of object reconstruction from cross sections is quite old and has been addressed in different forms. A lot of work has been done in 3D object reconstruction from planar cross sections (see, for example, [1–4]). The cross sections considered in these are generally contours of the objects that could be parallel or non-parallel as discussed by Boissonnat and Memari [5], and later by Liu et al. [6]. Hoppe et al. [7] discuss the problem of object reconstruction from a point cloud which is also of widespread interest. This problem has been analyzed from different perspectives. For example, Carr et al. [8] use radial basis functions for reconstruction. Amenta and Bern [9] use Voronoi filtering to generate surface from point clouds.

In the context of reconstruction from acoustic signals, most of the work focusses on reconstruction from cross section images (see, for example, the work by Zhang et al. [10]). In fact, acoustic images are obtained by interpolating intensities from planar acoustic beams arranged in a fan. A better algorithm can be designed to reconstruct the underlying object from original signals without relying on a simple interpolation based estimate.

Homotopy continuation is a powerful mathematical tool for robustly solving a complex system of equations (see Allgower and Georg [11]). Continuation based method suggested for surface reconstruction from planar contours by Shinagawa and Kunii [12] uses a straight line homotopy to generate smooth surface. Their method generates a minimal surface by finding optimal path in the toroidal graph representation. Berzin and Hagiwara [13] analyze minimal area criterion in surface reconstruction using homotopy and show that such criteria lead to defective surfaces. An isotopy based reconstruction scheme is proposed by Fujimura and Kuo [14], in which bifurcations are handled separately. In this paper we present a different reconstruction algorithm that utilizes continuous deformations of functions for tracing the reconstruction boundary. We develop homotopies other than linear homotopies that can generate smooth surface. The homotopies developed here are built to take advantage of the spatial arrangement of the signals.

This paper is organized as follows. In Sect. 2 we review the basic homotopy theory. Section 3 presents a brief overview of the acoustic signals from which a reconstruction is desired. Section 4 outlines our approach to reconstruction using homotopy deformation. We develop various homotopies suited to reconstruction. Section 5 is devoted to the reconstruction algorithm utilizing the concepts developed so far. In Sects. 6 and 7 we respectively present the results and time complexity of the presented algorithm. We conclude the discussion in Sect. 8.

## 2 Homotopy continuation

The central idea of the reconstruction algorithm presented here is *homotopy* (see Armstrong [15]) or *continuous deformation*. Two continuous functions, $f_0(\mathbf{x})$ and $f_1(\mathbf{x})$, $\mathbf{x} \in \mathbb{R}^N$, are called homotopic if one can be continuously deformed into the other. Such a deformation is called a homotopy $\mathcal{H}(\mathbf{x}, \lambda)$ (in parameter $\lambda \in \mathbb{R}$) between the two functions.

In other words, a family of continuous mappings

$$h_\lambda : X \mapsto Y, \quad \lambda \in [0, 1] \tag{1}$$

is called a homotopy if the function

$$\mathcal{H} : X \times [0, 1] \mapsto Y \tag{2}$$

defined by

$$\mathcal{H}(\mathbf{x}, \lambda) = h_\lambda(\mathbf{x}), \quad \mathbf{x} \in X, \ \lambda \in [0, 1] \tag{3}$$

is continuous. The maps $h_0$ and $h_1$ are called the *initial map* and the *terminal map* of the homotopy $h_\lambda$. A typical choice is a *linear homotopy* such as

$$\mathcal{H}(\mathbf{x}, \lambda) = (1 - \lambda) f_0(\mathbf{x}) + \lambda f_1(\mathbf{x}). \tag{4}$$

The use of deformations to solve non-linear system of equations gives robust results. A homotopy tries to solve a difficult problem with unknown solutions by starting with a simple problem with known solutions. Stable predictor-corrector and piecewise-linear methods for solving such problems exist (see Allgower and Georg [11]). The system $\mathcal{H}(\mathbf{x}, \lambda) = 0$ implicitly defines a curve or 1-manifold of solution points.

Given smooth $\mathcal{H}$ and existence of $u_0 \in \mathbb{R}^{N+1}$ such that $\mathcal{H}(u_0) = 0$ and $\operatorname{rank}(\mathcal{H}'(u_0)) = N$, there exists a smooth curve $\alpha \in J \mapsto c(\alpha) \in \mathbb{R}^{N+1}$ for some open interval $J$ containing zero such that for all $\alpha \in J$ (Allgower and Georg [11])

1. $c(0) = u_0$,
2. $\mathcal{H}(c(\alpha)) = 0$,
3. $\operatorname{rank}(\mathcal{H}'(c(\alpha))) = N$,
4. $c'(\alpha) \neq 0$.

The map $\mathcal{H}$ deforms $f_0$ to $f_1$ in a smooth fashion via the path $c$.

We use these concepts in Sect. 4 where we define non-linear, spline and shape preserving homotopies. Next section introduces the nature of acoustic signals and their spatial arrangement.

## 3 Acoustic signals

Multibeam sonar data acquisition results in huge amount of data in small time. The data is in the form of multiple beams of signals that are arranged in a particular geometry for an instrument. The MS70 Multibeam echo-sounder from Simrad is a 3D sonar where a total of 500 beams are arranged in a fashion such that an angular cone of 45° by 60° is spanned by a matrix of 20 × 25 beams. The echo-sounder operates on a frequency range of 75 to 112 kHz (see Ona et al. [16] for details).

Multibeam echo-sounders sample the space non-uniformly since the linear spacing between individual beams increases with distance along the beams. As a result, the objects far away from the instrument have a very coarse resolution in the sampled volume. Figure 1(a) shows a typical arrangement of the MS70 echo-sounder. A volume rendering of a single ping capturing a moving school of Sprat fish is shown in Fig. 1(b).

In order to reconstruct a surface representation of the objects imaged by the sonar, we formulate homotopies for beams. These are discussed in the next section.

## 4 Homotopic reconstruction

Consider a signal $S$ and its piecewise constant representation $G$. In other words, $G$ is a segmentation of $S$ with classes (or levels) $C_0, C_1, \ldots,$ and $C_{n-1}$. Let us denote by $\chi_k$ the characteristic function of $S$ for class $C_k$, such that

$$\chi_k = \begin{cases} 1 & \text{if } G = C_k, \\ 0 & \text{otherwise.} \end{cases} \tag{5}$$

The main idea behind reconstruction for any level $C_k$ using continuous deformations is to trace the path $\mathbf{c} = \ker(\mathcal{H}) = \{(\mathbf{x}, \lambda) : \mathcal{H} = 0\}$ between functions defined on any two consecutive signals (as shown in Fig. 2 in $\mathbb{R}^2$).

In order to be able to define homotopies between pairs of beams, we need to associate functions with each beam. Such

**Fig. 1** The MS70 echo-sounder. (**a**) MS70 beam configuration. (**b**) Volume rendering of sample data (high intensities in *red*)

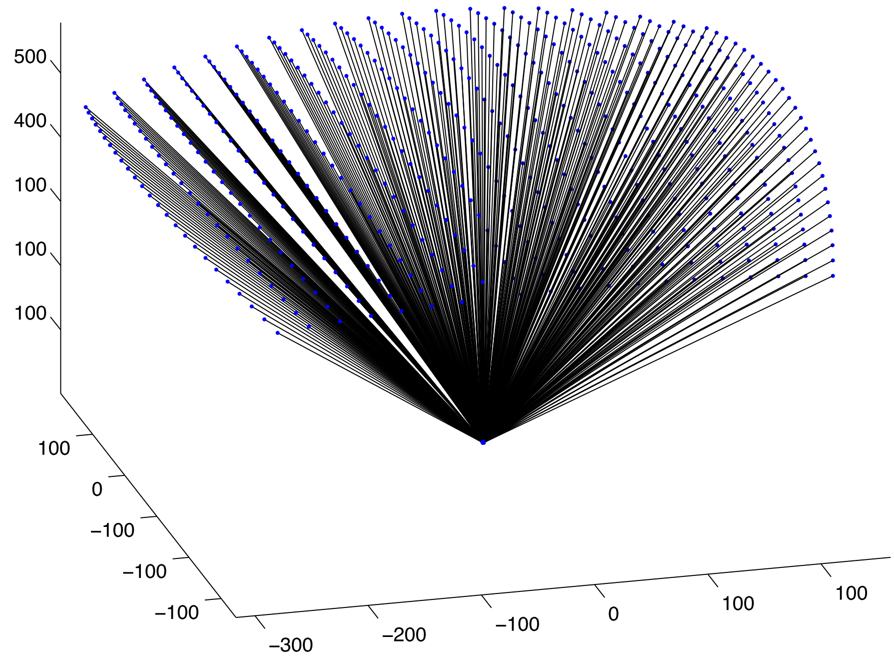


(a)

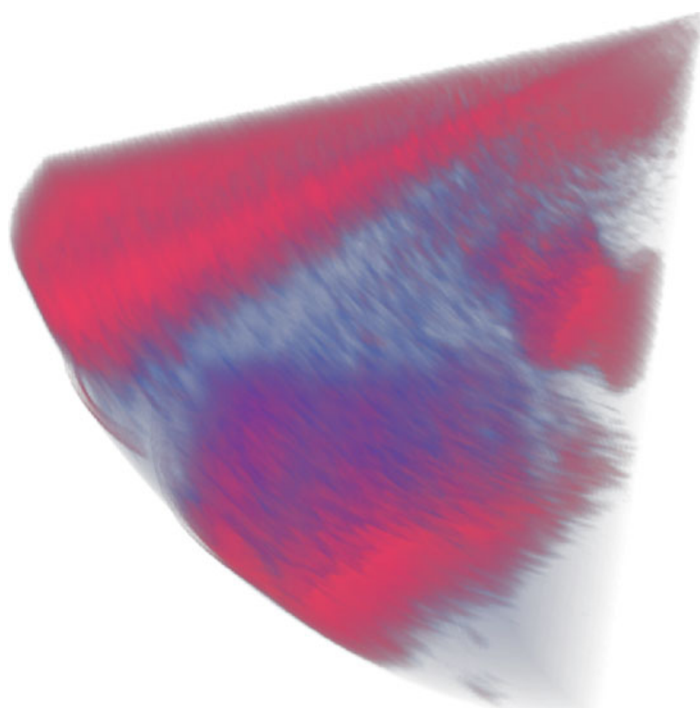

(b)

a *beam function* should completely describe the boundary, interior and exterior of regions belonging to any class $C_k$ along the respective beam. These regions are intervals in one-dimensional cross sections. The rest of the discussion applies to any class, therefore we drop the subscript $k$ for sake of simplicity of notation. Given roots $r_i, i \in [0, p-1]$ of the characteristic function $\chi$ of a beam, we define its beam function as a piecewise polynomial. This can be done by selecting slopes at the roots of the desired piecewise polynomial and enforcing continuity at borders of adjacent polynomials. The simplest piecewise polynomial exhibiting $C^1$ continuity is a piecewise

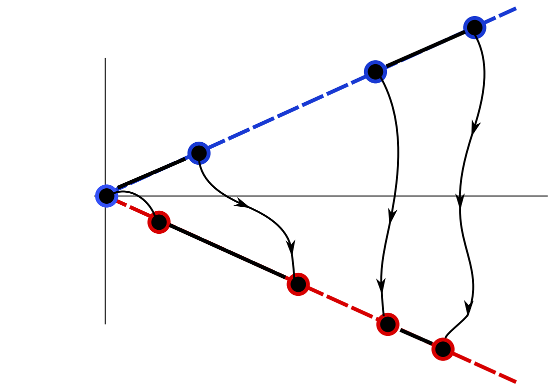

**Fig. 2** Homotopy path between two beams

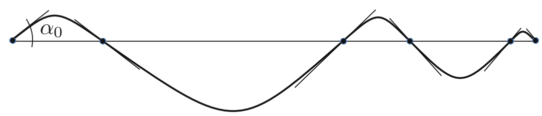


**Fig. 3** Piecewise quadratic function representing a beam

quadratic

$$f(r)=\sum_{i=0}^{p-2}\frac{\alpha_i(-r^2+r(r_i+r_{i+1})-r_ir_{i+1}))}{(r_{i+1}-r_i)}, \tag{6}$$

where $r$ is the distance along the beam, and $\alpha_i$ is the positive gradient $\left|\frac{\mathrm{d}f}{\mathrm{d}r}\right|_{r=r_i}$ defined as

$$\alpha_i=(-1)^{i+1}\alpha_0, \tag{7}$$

with $\alpha_0$ being a chosen positive slope at $r_0$. A quadratic polynomial also keeps the system simple to solve. Figure 3 illustrates such a beam function.

With this background, we define various homotopies in the following subsections.

### 4.1 Linear homotopy

Consider beam functions $f_j(r)$ and $f_{j+1}(r)$ for two consecutive beams with angles $\theta_j$ and $\theta_{j+1}$ respectively in the polar plane $(r,\theta)$. We define a homotopy $\mathcal{H}:\mathbb{R}^2\mapsto\mathbb{R}$ of smooth transition from $f_j(r)$ to $f_{j+1}(r)$ using a real parameter $\lambda\in[0,1]$ as

$$\mathcal{H}_j(r,\lambda)=(1-\lambda)f_j(r)+\lambda f_{j+1}(r), \tag{8}$$

where the parameter $\lambda$ is related to the angle $\theta$ as

$$\lambda=\frac{\theta-\theta_j}{\theta_{j+1}-\theta_j}. \tag{9}$$

Such an $\mathcal{H}$ is a linear homotopy that transforms $f_j(r)$ to $f_{j+1}(r)$ using a linear combination of these functions in parameter $\lambda$. We can now define a set of homotopies that

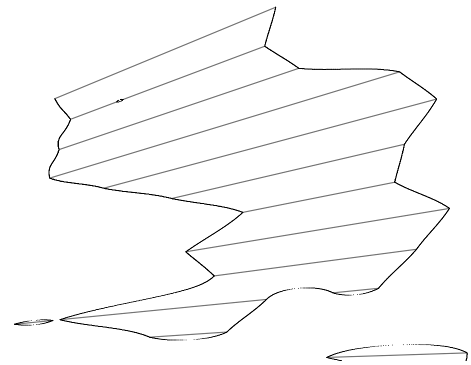

**Fig. 4** Reconstruction using linear homotopy. Reconstructed object (with more than one connected components) boundary connects the end points of radial cross sections (*in gray*)

reconstructs the underlying object from a set of beams as the set $\mathbf{H}=\{\mathcal{H}_j\}$ where each homotopy $\mathcal{H}_j$ is defined for a pair of beam signals $S_j$ and $S_{j+1}$.

A reconstruction from $\mathbf{H}$ is then given by the curve $\mathbf{c}=\ker(\mathbf{H})=\bigcup_{j\in J}\ker(\mathcal{H}_j)$. Figure 4 shows part of the reconstruction of a set of radial beams.

**Proposition 1** *$\mathbf{H}$ defined in (8) results in a piecewise non-linear curve $\mathbf{c}$ that is only $C^0$ in $\theta$.*

*Proof* We prove this by showing that

1. $\mathbf{c}$ is $C^0$ at $(r_i,\theta_{j+1})$[1], and
2. $\mathbf{c}$ is not $C^1$ at $(r_i,\theta_{j+1})$.

For part 1, it is sufficient to show that $\mathcal{H}_j(r_i,\theta_{j+1})=\mathcal{H}_{j+1}(r_i,\theta_{j+1})$. From (8),

$$\mathcal{H}_j(r_i,\theta_{j+1})=f_{j+1}(r_i),\quad \text{and}$$
$$\mathcal{H}_{j+1}(r_i,\theta_{j+1})=f_{j+1}(r_i).$$

Therefore, $\mathbf{c}$ is $C^0$.

For part 2, consider the tangent at any point $(r,\theta)$ for $\mathcal{H}_j$:

$$\begin{aligned}T_j&=\left(\frac{\partial\mathcal{H}_j}{\partial r},\frac{\partial\mathcal{H}_j}{\partial\theta}\right)\\&=\left((1-\lambda)f_j'(r)+\lambda f_{j+1}'(r),\frac{-f_j(r)+f_{j+1}(r)}{\Delta\theta_j}\right),\end{aligned} \tag{10}$$

where $\Delta\theta_j=(\theta_{j+1}-\theta_j)$. At $r=r_i$, we note that

$$\begin{aligned}&\lim_{\theta\to\theta_{j+1}^-}T_{j+1}=\left(f_{j+1}'(r_i),\frac{-f_j(r_i)+f_{j+1}(r_i)}{\Delta\theta_j}\right)\quad\text{and}\\&\lim_{\theta\to\theta_{j+1}^+}T_{j+1}=\left(f_{j+1}'(r_i),\frac{-f_{j+1}(r_i)+f_{j+2}(r_i)}{\Delta\theta_{j+1}}\right).\end{aligned} \tag{11}$$

[1] This point belongs to $\mathbf{c}$ since $r_i$ is a zero of $f_{j+1}(r)$ by construction.

Therefore, $\lim_{\theta\to\theta_{j+1}^-} T_{j+1} \neq \lim_{\theta\to\theta_{j+1}^+} T_{j+1}$, and $\mathbf{c}$ is not $C^1$. This shows that $\mathbf{c}$ is only $C^0$ in $\theta$. □

Therefore, we seek a homotopy that preserves tangent slopes at the joins. This leads us to the introduction of *non-linear homotopy*.

### 4.2 Non-linear homotopy

The curve $\mathbf{c} = \ker(\mathbf{H})$ resulting from (8) is a piecewise smooth curve in $\mathbb{R}^2$. We are interested in at least a $C^1$ continuous curve generated by a homotopy function. Let us consider the following non-linear homotopy in $\lambda$:

$$\mathcal{H}_j(r,\lambda,\eta) = (1-\lambda)^\eta f_j(r) + \lambda^\eta f_{j+1}(r). \tag{12}$$

Figure 5 shows a reconstruction using the non-linear homotopy defined by (12).

**Proposition 2** *For $\eta > 1$, $\ker(\mathbf{H})$ generates at least a $C^1$ curve in $\theta$ for constant angular spacing of beams.*

*Proof* We prove this by showing that

1. $\mathbf{c}$ is $C^0$ at $(r_i, \theta_{j+1})$, and
2. $\mathbf{c}$ is $C^1$ at $(r_i, \theta_{j+1})$ for uniform angular spacing of beams.

As before, we can prove part 1 using (8) by showing that $\mathcal{H}_j(r_i,\theta_{j+1}) = \mathcal{H}_{j+1}(r_i,\theta_{j+1})$.

For part 2, we again consider the tangent at any point $(r,\theta)$ for $\mathcal{H}_j$:

$$\begin{aligned} T_j &= \left(\frac{\partial\mathcal{H}_j}{\partial r}, \frac{\partial\mathcal{H}_j}{\partial\theta}\right) \\ &= \Bigg((1-\lambda)^\eta f_j'(r) + \lambda^\eta f_{j+1}'(r), \\ &\qquad \frac{-\eta(1-\lambda)^{\eta-1} f_j(r) + \eta\lambda^{\eta-1} f_{j+1}(r)}{\Delta\theta_j}\Bigg). \end{aligned}$$

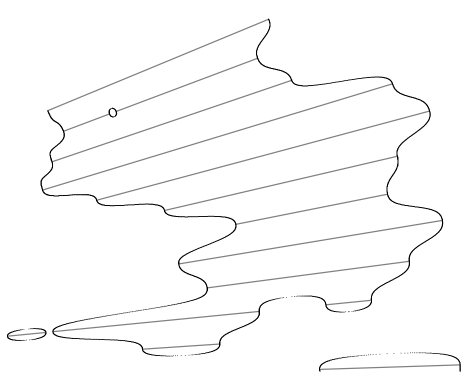

**Fig. 5** Reconstruction using non-linear homotopy ($\eta = 2$) from the same set of radial cross sections. Staircase effect is prominent in this reconstruction

At $r = r_i$, we note that

$$\begin{aligned} &\lim_{\theta\to\theta_{j+1}^-} T_{j+1} = \left(f_{j+1}'(r_i), \frac{\eta f_{j+1}(r_i)}{\Delta\theta_j}\right) \quad \text{and} \\ &\lim_{\theta\to\theta_{j+1}^+} T_{j+1} = \left(f_{j+1}'(r_i), \frac{-\eta f_{j+1}(r_i)}{\Delta\theta_{j+1}}\right). \end{aligned} \tag{13}$$

If $\Delta\theta = \Delta\theta_j = \Delta\theta_{j+1}$ is the constant angular spacing between the beams, then

$$\lim_{\theta\to\theta_{j+1}^-} T_{j+1} = \lim_{\theta\to\theta_{j+1}^+} T_{j+1}.$$

This shows that $\mathbf{c}$ is at least $C^1$ in $\theta$. Further, it can also be shown that the slope at beam end is normal to the radial line at angle $\theta_{j+1}$. This is left as an exercise to the reader. □

A non-linear homotopy is a general case of the linear homotopy. This class of deformations can be extended to higher dimensions in a straightforward manner. A formulation in $\mathbb{R}^3$ for an arrangement of beams shown in Fig. 6 can be made as a two-parameter homotopy in $\alpha$ and $\beta$ as

$$\begin{aligned} \mathcal{H}_{j,k}(r,\alpha,\beta,\eta,\zeta) = f_{j,k}(r)&(1-\alpha)^\eta(1-\beta)^\zeta \\ &+ f_{j,k+1}(r)(1-\alpha)^\eta\beta^\zeta \\ &+ f_{j+1,k}(r)\alpha^\eta(1-\beta)^\zeta \\ &+ f_{j+1,k+1}(r)\alpha^\eta\beta^\zeta, \end{aligned} \tag{14}$$

where $\alpha$ and $\beta$ are linearly related to the inclination $\theta$ and azimuth $\phi$ in a spherical coordinate system $(r,\theta,\phi)$ (similarly to (9) in $\mathbb{R}^2$). The two-parameter homotopy (14) can also be written as a tensor product of one-parameter homotopies.

For the $\mathcal{H}_{j,k}$ defined above, it can be shown that the surface $\mathcal{H} = 0$ is $C^1$ continuous for $\eta > 1$, $\zeta > 1$. For $\eta = 1$ and $\zeta = 1$, $\mathcal{H}_{j,k}$ reduces to a linear homotopy.

A non-linear homotopy is continuous at joins and satisfies all the required criteria; however, the reconstruction looks unnatural due to the fact that the tangents at the joins are always orthogonal to the respective beams (see Fig. 5). This constrains the solution to a small class of possible reconstructions. In the next subsection, we relax the tangent constraint that gives rise to the *cubic spline homotopy*.

**Fig. 6** Top view of beam arrangement in $\mathbb{R}^3$. Each dot represents a beam orthogonal to the plane of the paper

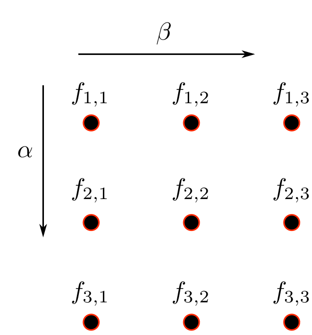

### 4.3 Cubic spline homotopy

Consider $N$ radial beam functions $\{f_j(r)\}$, $j \in [0, N-1]$ in the polar plane $(r, \theta)$. While deriving the necessary conditions, we replace the local parameter $\lambda$ by its global counterpart $\theta$. These two are related by (9). We construct homotopies $\mathcal{H}_j$ between $f_j$ and $f_{j+1}$ such that the following conditions are met:

1. For any homotopy, the initial and terminal maps are satisfied:

$$\mathcal{H}_j(r, \theta_j) = f_j(r), \quad \text{and} \quad \mathcal{H}_j(r, \theta_{j+1}) = f_{j+1}(r), \tag{15}$$

   for $j \in [0, N-2]$.
2. The first derivatives $\partial \mathbf{H}(r,\theta)/\partial\theta$ at the boundary of any two successive homotopies match

$$\lim_{\theta \to \theta_{j+1}^-} \frac{\partial \mathcal{H}_j(r,\theta)}{\partial \theta} = \lim_{\theta \to \theta_{j+1}^+} \frac{\partial \mathcal{H}_{j+1}(r,\theta)}{\partial \theta}, \tag{16}$$

   for $j \in [0, N-3]$.
3. The second derivatives $\partial^2 \mathbf{H}(r,\theta)/\partial\theta^2$ at the boundary of any two successive homotopies match

$$\lim_{\theta \to \theta_{j+1}^-} \frac{\partial^2 \mathcal{H}_j(r,\theta)}{\partial \theta^2} = \lim_{\theta \to \theta_{j+1}^+} \frac{\partial^2 \mathcal{H}_{j+1}(r,\theta)}{\partial \theta^2}, \tag{17}$$

   for $j \in [0, N-3]$.

We start with a general cubic homotopy in $\theta$ of the form

$$\mathcal{H}_j(r,\theta) = \sum_{i=0}^{3} g_{j,i}(r)(\theta - \theta_j)^i, \tag{18}$$

with unknown coefficient functions $g_{j,i}$. We note the following partial derivatives of $\mathcal{H}_j(r,\theta)$ w.r.t $\theta$:

$$\frac{\partial \mathcal{H}_j(r,\theta)}{\partial \theta} = \sum_{i=1}^{3} i g_{j,i}(r)(\theta - \theta_j)^{i-1}, \quad \text{and} \tag{19}$$

$$\frac{\partial^2 \mathcal{H}_j(r,\theta)}{\partial \theta^2} = \sum_{i=2}^{3} i(i-1) g_{j,i}(r)(\theta - \theta_j)^{i-2}. \tag{20}$$

Note that in the above conditions, we are not concerned with the derivatives of $\mathbf{H}$ w.r.t. $r$ since these have no influence on continuity of $\mathbf{c}$ w.r.t. $\theta$. Continuity of $\mathbf{c}$ w.r.t. $r$ depends on the choice of beam functions $f(r)$. Conditions (15), (16) and (17) result in the following linear system (argument $r$ of $g$'s and $f$'s is removed for space consideration):

$$\begin{aligned}
&g_{j,0} = f_j, \quad \text{for } j \in [0, N-2],\\
&g_{j,0} + g_{j,1}\Delta + g_{j,2}(\Delta\theta_j)^2 + g_{j,3}(\Delta\theta_j)^3 = f_{j+1},\\
&\quad \text{for } j \in [0, N-2],\\
&g_{j,1} + 2g_{j,2}\Delta\theta_j + 3g_{j,3}(\Delta\theta_j)^2 = g_{j+1,1},\\
&\quad \text{for } j \in [0, N-3],\\
&g_{j,2} + 3g_{i,3}\Delta\theta_j = g_{j+1,2}, \quad \text{for } j \in [0, N-3].
\end{aligned} \tag{21}$$

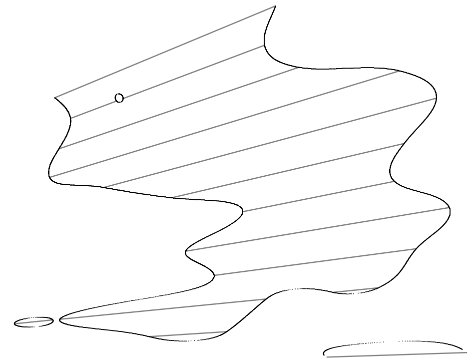

**Fig. 7** Reconstruction using spline homotopy using same set of radial cross sections. Spline reconstruction clearly shows smoothness of the reconstruction

Since system (21) is devoid of two conditions, we enforce free boundary condition $\partial^2\mathcal{H}(r,\theta)/\partial\theta^2 = 0$ at $\theta_0$ and $\theta_{N-1}$. This yields the following two linear equations:

$$g_{0,2} = 0 \quad \text{and} \quad g_{N-2,2} + 3g_{N-2,3}\Delta\theta_j = 0. \tag{22}$$

The system formed by (21) and (22) has the form $A\mathbf{x} = B$. The coefficients $g_{j,i}$ are functions of $f_j$. The homotopy (18) can be rewritten in terms of the local homotopy variable $\lambda$. Figure 7 shows a reconstruction using the developed cubic spline homotopy. It is possible to extend the single-parameter cubic spline homotopy to a two-parameter spline homotopy for a reconstruction in $\mathbb{R}^3$ via the tensor product.

With the cubic homotopy it is possible to have a continuous reconstruction with no restriction on tangents at the beam ends; however, the resulting surface suffers from undesirable extremum points between places of high difference in radial distance between beam boundaries (see Fig. 8). This is due to the fact that it is not always possible to have $C^2$ continuity while maintaining monotonicity [17, 18]. To overcome this problem, we introduce a shape preserving $C^1$ homotopy in the next subsection.

### 4.4 Shape preserving homotopy

Monotonicity preserving splines overcome the problem associated with cubic splines. Späth [19] introduced generalized exponential splines in tension that were further studied by Pruess [20] and others. These splines are piecewise exponential curves joining together to form a smooth curve in tension. The tension parameters, however, must be selected by some heuristic based on the gradient of the data points or

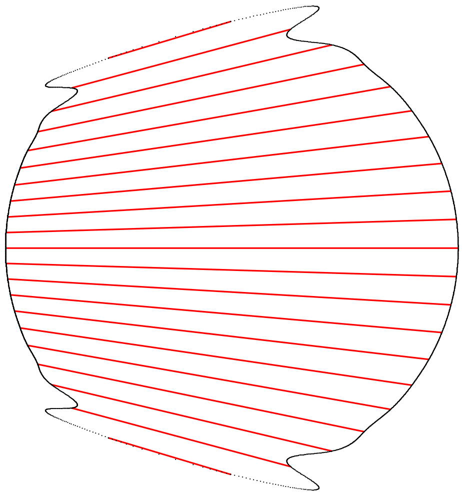

**Fig. 8** Cubic spline reconstruction of a circle from a set of radial cross sections showing undesirable bulge on the sides

otherwise. Further, computation of tension splines is expensive due to evaluation of hyperbolic functions. The computation is also sensitive to the choice of tension parameters. This is specially true for very small tension parameters causing underflow of machine precision and for very large tension parameters causing overflow of machine precision [21].

Monotonicity can be attained by sacrificing smoothness while still using polynomials. We develop a $C_1$ homotopy based on the monotonic splines of Hyman [17]. This requires availability of derivatives $\partial\mathcal{H}_j(r,\lambda)/\partial\lambda$ at $\lambda=0$. A monotone homotopy can be written in terms of Hermite basis functions as

$$\begin{aligned}\mathcal{H}_j(r,\lambda) &= \left(1-3\lambda^2+2\lambda^3\right)f_j(r)+\left(3\lambda^2-2\lambda^3\right)f_{j+1}(r)\\ &\quad+\left(\lambda-2\lambda^2+\lambda^3\right)\left[\frac{\partial\mathcal{H}_j(r,\lambda)}{\partial\lambda}\right]_{\lambda=0}\\ &\quad+\left(\lambda^3-\lambda^2\right)\left[\frac{\partial\mathcal{H}_{j+1}(r,\lambda)}{\partial\lambda}\right]_{\lambda=0}.\end{aligned}\tag{23}$$

The derivatives $\partial\mathcal{H}_j/\partial\lambda$ appearing in (23) enforce piecewise monotonicity in **c**. The de Boor and Swartz [22] piecewise monotonicity range can be extended for functions as

$$0\le\dot{f}_j\le 3\min(\triangle f_j,\triangle f_{j+1}),\tag{24}$$

where $\triangle f_j=(f_{j+1}-f_{j-1})$ and $\dot{f}_j$ denotes the required derivative. Starting with an approximation of the derivatives (either from a spline representation or differencing), these are then projected into the monotonicity region defined by (24) according to

$$\dot{f}_j=\begin{cases}\min\bigl(\max(0,\dot{f}_j),3\min(|\triangle f_j|,|\triangle f_{j+1}|)\bigr)\\ \max\bigl(\min(0,\dot{f}_j),-3\min(|\triangle f_j|,|\triangle f_{j+1}|)\bigr).\end{cases}\tag{25}$$

The reader is referred to work by Hyman [17] for a detailed discussion on this. The constrained derivatives can be used in (23). The derivatives can only be computed numerically. Other procedures outlined by Costantini and Morandi [23] and Wolberg and Alfy [18] employ optimizations to compute the derivatives. A two-parameter family of monotone shape-preserving homotopy can be formulated, as before, via tensor product. The result of monotone reconstruction is shown in Sect. 6.

A reconstruction algorithm based on the developed homotopies is presented next.

## 5 Reconstruction algorithm

The MS70 sonar gives a 3D view of the ensonified volume as shown in Fig. 1(b). The received signal represents the raw acoustic backscatter from the seabed and the fish school. In order to infer useful object information from the signals, these must first be corrected for spreading and absorption losses during acoustic wave propagation (see Simmonds and MacLennan [24] for details). The resulting *Volume backscattering strength* $S_v$ values can then be used for analysis.

### 5.1 Characteristic function generation

To generate a good segmentation, anisotropic diffusion by Perona and Malik [25] may be performed on the $Sv$ signals. The usual practice is to binary-segment the signals by choosing a suitable threshold value depending on the species of the schooling fish seen in the volume. The threshold should be chosen so as to eliminate as much of the background and instrument noise as possible (see Simmonds and MacLennan [24]).

Following is the general procedure adopted to generate characteristic signals from raw acoustic signals:

1. Perform anisotropic diffusion filtering on the input volume $V_i$ to generate $V_{\mathrm{diff}}$.
2. Generate a binary volume $V_{\mathrm{bin}}$ by using a threshold value $S_{\mathrm{thres}}$.
3. Close holes in $V_{\mathrm{bin}}$ by 3D morphological closing (see Soille [26]). Isolated voxels are eliminated by a morphological opening.
4. Label the resulting volume, as $V_{\mathrm{seg}}$, into different connected components (see Gonzalez and Woods [27]).
5. Select a component or combine several components from $V_{\mathrm{seg}}$ into $V_\chi$ that represent the object to reconstruct. This is a binary volume representing the characteristic signal of the desired object.

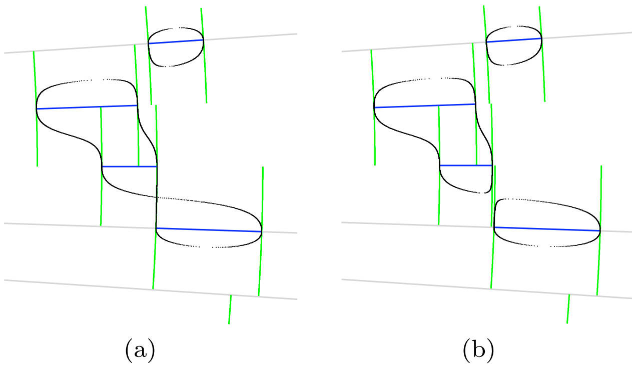


**Fig. 9** Handling cross-overs in the homotopy solution. Radial cross sections are shown in gray with location of roots along each radial line marked in green. A root on any radial line is projected onto adjacent radial lines for clarity. (**a**) Singularity in the path. (**b**) Avoiding singularity by perturbation of roots

5.2 Solution of homotopy

Starting with a binary volume $V_\chi$ of size $M \times N \times R$, where $R$ is the number of samples along a signal beam, we associate beam functions with all $MN$ beams according to (6). A system of $(M-1) \times (N-1)$ homotopies is formulated.

The reconstruction $\mathcal{H} = 0$ traces the homotopy path without any problem except at places where the path encounters a singularity (self-intersection) in between the initial and terminal maps for $\lambda \in (0, 1)$. In such a case, the path becomes a non-manifold, as illustrated in Fig. 9(a). Such a case can be avoided by first identifying a root $r_k$ of any one of the beam functions that causes a singularity, and perturbing it in such a way that the singularity in the path is avoided, as shown in Fig. 9(b).

The set of homotopies can be solved to find points belonging to ker($\mathbf{H}$) that lie on the boundary of the reconstruction. An analytical solution to $\mathbf{H} = 0$ is not always possible, and a computational solution for all $\lambda \in [0, 1]$ is not realizable. Therefore, we construct a scalar field of $\mathbf{H}$ on a sampled grid. The homotopy path is then found by tracing zero level set of the scalar field.

## 6 Results

We present results of our reconstruction algorithm here. Although the reconstruction algorithm operates in the beam space, for sake of clarity we show all the 2D illustrations in polar coordinates. It must be noted that a coordinate transformation from beam space to spherical coordinates is needed only before the level set extraction and not before.

The raw data is shown in Fig. 1(b) where the high intensity regions of the ensonified volume are rendered in red. These regions are mainly the fish school, seabed and noise at the top. We show a slice of the raw volume in Fig. 10(a).

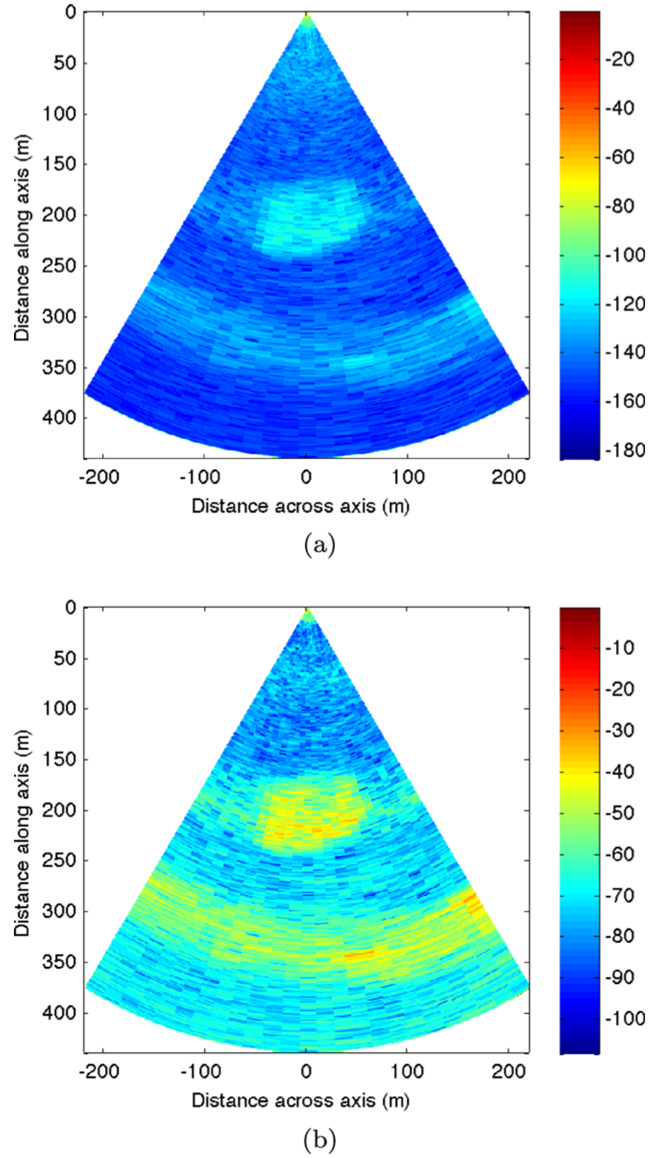


**Fig. 10** Intensity correction on raw volume. (**a**) Sector of the volume showing raw intensities. (**b**) Volume corrected for spreading and absorption losses

Note that the intensity of the target diminishes as the distance from the transducer (located at the tip of the sector) increases. Figure 10(b) shows volume compensated for acoustic losses due to spreading and absorption. The intensities after compensation are distributed evenly (for example, typical fish school echo strength values are around $-60$ dB).

A threshold of $-62$ dB removes much of the background noise in this case. Combined characteristic functions of the seabed and the fish school are shown in Fig. 11. In the figure, thick black lines show the ranges where the characteristic function takes a value of 1.

A full reconstruction in $\mathbb{R}^3$ is shown in Fig. 12. Here, different connected components are colored differently and the noise component is not considered during reconstruction.

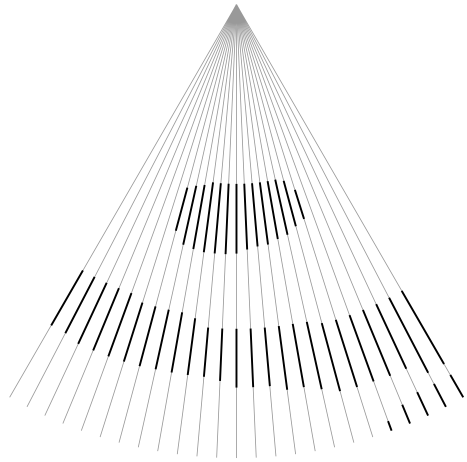

**Fig. 11** Combined characteristic signal for seabed and fish school. Complete radial lines are shown in *gray* while the cross section is shown in *black*

The seabed is shown in brown, while the fish school is colored in light blue. The difference in the reconstructions computed via the four homotopies is apparent and shows that the shape preserving monotone homotopy outperforms the others. A linear homotopy renders the reconstruction piecewise $C^0$ that does not look natural, while the non-linear homotopy introduces staircase like artifacts. The cubic homotopy on the other hand produces large variations in the surface at the sides causing undesired bumps.

With the real signals, it is not possible to quantify accuracy of the suggested homotopies. Therefore, we perform simulation tests described next.

### 6.1 Accuracy comparison

In order to evaluate the relative performance of the suggested homotopies, we reconstruct various simple geometric primitives. We compare the reconstructed surfaces with the respective primitives by means of certain measures. In all the simulations, we use a set of $20 \times 25$ beams of length 100 units and spanning an angular volume of $45° \times 60°$ (see Fig. 13). A primitive is placed symmetrically in the spanned volume such that the center of the primitive is halfway from the apex of the sonar. With the given beam density, it must be noted that any primitive is sampled sparsely (i.e., not following the Nyquist criterion), and therefore it is not possible to completely recover an object with all details. This represents the practical case with acoustic instruments where beam density is constrained by various physical factors and cannot be arbitrarily increased. Also, beneath the water, objects to be mapped have unknown geometry and location. In our analysis, we use several parameters for shape comparison. Two simple parameters are ratio of the two surface areas $A_r/A_o$ and ratio of the two volumes $V_r/V_o$. Further, we measure the reconstruction error by means of the *symmetrical Hausdorff distance* which is a good measure of the distance between two manifolds (see Aspert et al. [28]).

Symmetrical Hausdorff distance, $d_H$, between two surfaces $M_0$ and $M_1$ is given by

$$d_H(M_0, M_1) = \max\left\{\sup_{x_0\in M_0}\inf_{x_1\in M_1} d(x_0,x_1),\ \sup_{x_1\in M_1}\inf_{x_0\in M_0} d(x_0,x_1)\right\}, \tag{26}$$

where $d(\cdot,\cdot)$ is an appropriate metric for measuring distance between two points in a metric space. $d_H(M_0, M_1)$ measures the maximum possible distance that will be required to travel from surface $M_0$ to $M_1$. We compute this metric and use it to quantify the error in reconstruction of a phantom surface. Similarly, a mean Hausdorff error $\overline{d_H}$ [28] can also be defined as

$$\overline{d_H}(M_0, M_1) = \max\left\{\frac{1}{A_{M_0}}\iint_{x_0\in M_0} d(x_0, M_1)\,\mathrm{d}M_0,\ \frac{1}{A_{M_1}}\iint_{x_1\in M_1} d(x_1, M_0)\,\mathrm{d}M_1\right\}, \tag{27}$$

where $A_{M_0}$ and $A_{M_1}$ denote the area of $M_0$ and $M_1$ respectively and $\mathrm{d}M_0$ and $\mathrm{d}M_1$ denote a differential area element on $M_0$ and $M_1$ respectively. In the following tables, a % refers to the relative Hausdorff distance measured as the percentage of the model bounding box diagonal.

The first primitive we consider is a sphere of radius 10 units. The reconstructions are shown in Fig. 14 with the sphere drawn in wireframe. It can be seen that linear and monotone reconstructions produce satisfactory results, since both are shape preserving. Non-linear reconstruction produces the ringing effect while the cubic homotopy produces bumps in the surface at the sides. Table 1 shows the three shape measures for these reconstructions. The reconstructed volume and surface area for cubic reconstruction are larger than that of the sphere. The best ratios are obtained for the shape preserving $C^1$ reconstruction with an exception of the volume ratio for cubic reconstruction. The Hausdorff distances (both maximum and mean) are very high for the cubic reconstruction indicating that the reconstructed surface has regions of high deviation from the phantom sphere surface. The minimum error is obtained for the monotone reconstruction indicating that the two surfaces are closest to each other.

Next we consider a cube of side length 20 units. A cube is an interesting primitive since the surface is only $C^0$, therefore a linear reconstruction gives a shape that is closest to it (see Fig. 15). The surface area ratio shown in Table 2 indicates that a better reconstruction is monotone. The volume

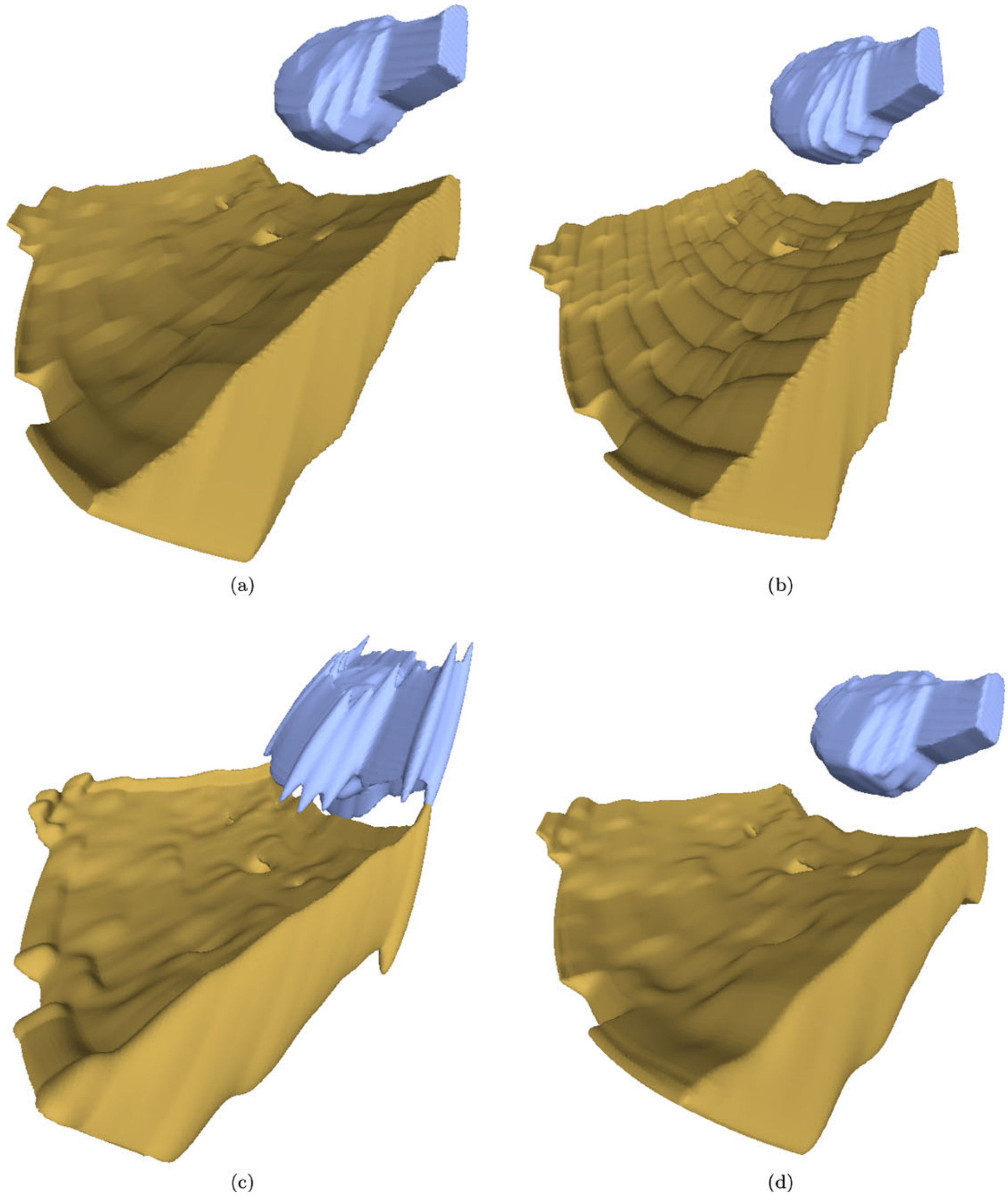


**Fig. 12** Homotopy reconstruction of moving school of Sprat. (**a**) Linear homotopy. (**b**) Non-linear homotopy with $\eta = 2$. (**c**) Spline homotopy. (**d**) Shape preserving homotopy

ratios show that the reconstructed surface is an underestimation of the primitive except for the cubic reconstruction that has overhangs in the reconstruction. The Hausdorff error gives a clear indication that the cubic reconstruction deviates most from the phantom surface while the monotone reconstruction deviates the least.

Next we experiment with a cone of semi-angle 30° and height 20 units, and a cylinder of radius 10 units and height 20 units. The reconstructions for these primitives are shown in Figs. 16 and 17, respectively. These surfaces have both planar and curved sections. As seen in the previous cases, the linear and monotone reconstructions perform better in this case as well with area and volume ratios closest to one, and the least Hausdorff errors for the monotone reconstruction (as shown in Tables 4 and 3).

So far the primitives considered here are convex in geometry. Lastly, we consider a torus for reconstruction to show that a non-convex geometry with holes can be reconstructed in a similar fashion and poses no limitation on the algorithm developed here. Here again, the accuracy measures indicate

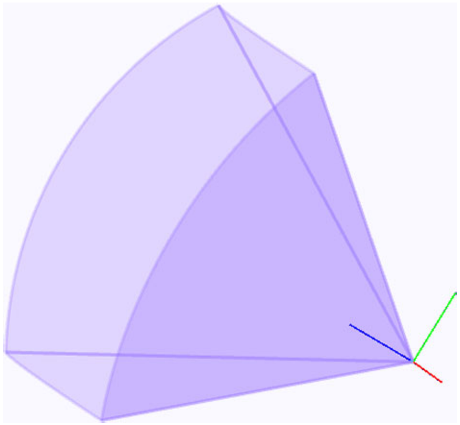

**Fig. 13** The simulation test bed consisting of a set of simulated sonar beams (20 × 25) in a frustum of angular volume of 45° × 60°. The sonar beams emerge from the origin denoted by the intersection of the coordinate axes

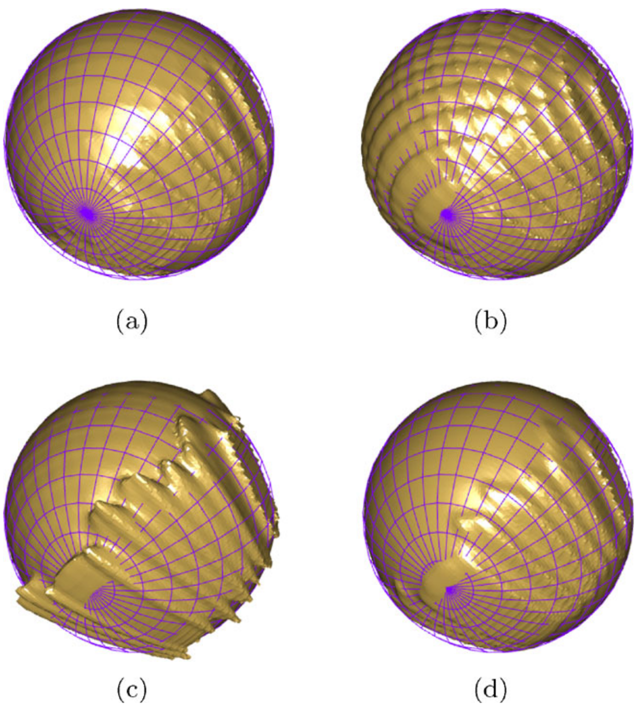

**Fig. 14** Homotopy reconstruction of a sphere. (**a**) Linear homotopy. (**b**) Non-linear homotopy with $\eta = 2$. (**c**) Spline homotopy. (**d**) Shape preserving homotopy

**Table 1** Reconstruction performance with sphere

| Reconstruction | $A_r/A_o$ | $V_r/V_o$ | $d_H$ (%) | $\overline{d_H}$ (% ) |
|---|---|---|---|---|
| Linear ($C^0$) | 0.963 | 0.865 | 4.340 | 0.896 |
| Non-linear ($C^{\eta-1}$) | 0.988 | 0.885 | 4.686 | 0.920 |
| Cubic ($C^2$) | 1.384 | 1.051 | 8.933 | 1.467 |
| Monotone ($C^1$) | 1.011 | 0.932 | 3.891 | 0.659 |

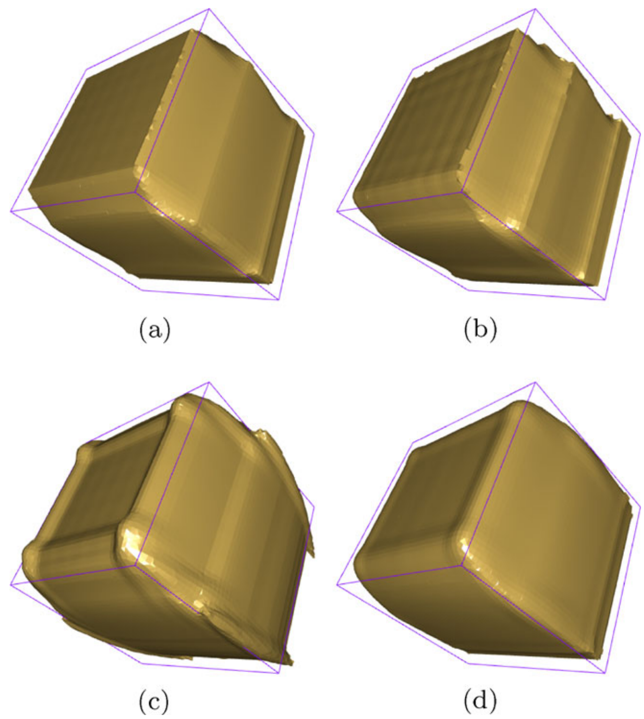

**Fig. 15** Homotopy reconstruction of a cube. (**a**) Linear homotopy. (**b**) Non-linear homotopy with $\eta = 2$. (**c**) Spline homotopy. (**d**) Shape preserving homotopy

**Table 2** Reconstruction performance with cube

| Reconstruction | $A_r/A_o$ | $V_r/V_o$ | $d_H$ (%) | $\overline{d_H}$ (% ) |
|---|---|---|---|---|
| Linear ($C^0$) | 0.880 | 0.902 | 6.206 | 0.778 |
| Non-linear ($C^{\eta-1}$) | 0.899 | 0.916 | 6.596 | 0.975 |
| Cubic ($C^2$) | 1.116 | 1.038 | 13.467 | 1.173 |
| Monotone ($C^1$) | 0.912 | 0.957 | 4.754 | 0.647 |

that the monotone reconstruction is closest to the original torus model. Also looking at the results, the cubic reconstruction shows the presence of unwanted peaks.

The simulations shown here clearly indicate superiority of the monotone reconstruction compared to other homotopies. This is supported by the least Hausdorff errors in case of monotone homotopic reconstruction. The main advantage comes with suppression of bumps while still remaining smooth. The volume ratio does not seem to be the best indicator of the geometry of the reconstructed surface. Depending on the arrangement of intersecting beams, in some cases the deviation of this measure from one is less than such a deviation in other methods. This indicates that in those cases the cubic method performs better than other methods, which is clearly not the case as shown by the area ratio and the Hausdorff error metrics. If the geometry of the original object is known a priori, a suitable homotopy can be chosen. It

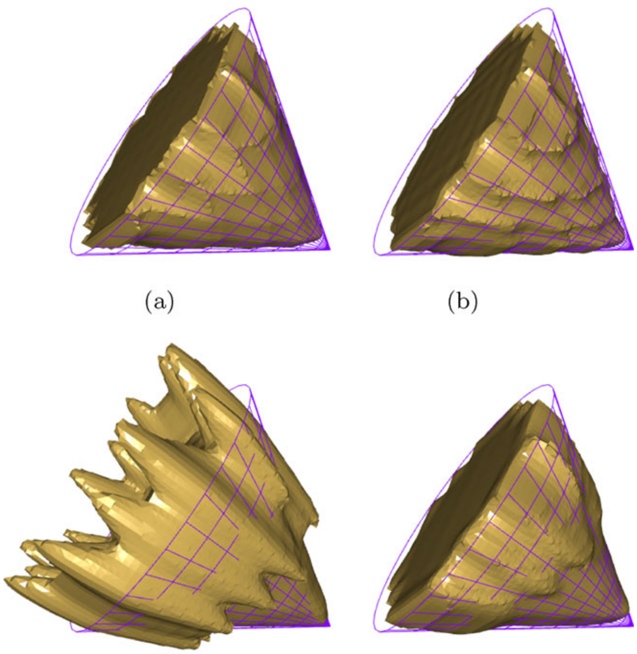

(a) (b) (c) (d)

**Fig. 16** Homotopy reconstruction of a cone. (**a**) Linear homotopy. (**b**) Non-linear homotopy with $\eta = 2$. (**c**) Spline homotopy. (**d**) Shape preserving homotopy

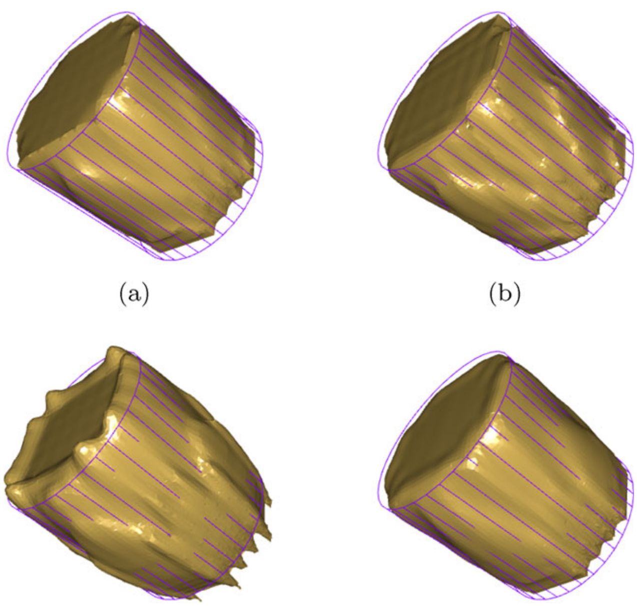

(a) (b) (c) (d)

**Fig. 17** Reconstruction of a cylinder. (**a**) Linear homotopy. (**b**) Non-linear homotopy with $\eta = 2$. (**c**) Spline homotopy. (**d**) Shape preserving homotopy

must be noted that an increase in beam density will increase the accuracy of reconstruction.

To our knowledge, we presented an algorithm for direct reconstruction of a surface from one-dimensional cross sections embedded in 3D and the existing methods of surface reconstruction from acoustic cross sections rely on interpolation to first compute an acoustic image/volume before deriving a surface. Methods like the level set method operate on such a volume to reconstruct an object using a deformable surface. A comparison of volume-based methods with the proposed method will be not be justified due to different input types of these methods. In the next section we present the complexity of the presented algorithm.

**Table 3** Reconstruction performance with cylinder

| Reconstruction | $A_r/A_o$ | $V_r/V_o$ | $d_H$ (%) | $\overline{d_H}$ (%) |
|---|---|---|---|---|
| Linear ($C^0$) | 0.917 | 0.913 | 4.511 | 0.544 |
| Non-linear ($C^{\eta-1}$) | 0.944 | 0.926 | 4.862 | 0.731 |
| Cubic ($C^2$) | 1.192 | 1.063 | 15.674 | 1.094 |
| Monotone ($C^1$) | 0.954 | 0.975 | 4.104 | 0.377 |

**Table 4** Reconstruction performance with cone

| Reconstruction | $A_r/A_o$ | $V_r/V_o$ | $d_H$ (%) | $\overline{d_H}$ (% ) |
|---|---|---|---|---|
| Linear ($C^0$) | 0.859 | 0.858 | 8.012 | 0.950 |
| Non-linear ($C^{\eta-1}$) | 0.885 | 0.876 | 7.640 | 0.998 |
| Cubic ($C^2$) | 1.460 | 1.186 | 19.049 | 2.509 |
| Monotone ($C^1$) | 0.901 | 0.944 | 6.979 | 0.641 |

**Table 5** Reconstruction performance with torus

| Reconstruction | $A_r/A_o$ | $V_r/V_o$ | $d_H$ (%) | $\overline{d_H}$ (% ) |
|---|---|---|---|---|
| Linear ($C^0$) | 0.967 | 0.820 | 4.309 | 0.860 |
| Non-linear ($C^{\eta-1}$) | 0.984 | 0.842 | 4.514 | 0.782 |
| Cubic ($C^2$) | 1.632 | 1.092 | 8.852 | 1.818 |
| Monotone ($C^1$) | 1.000 | 0.889 | 3.847 | 0.625 |

## 7 Time complexity

The time complexity of the homotopy reconstruction algorithm depends on the number of linear cross sections $n_{\text{sec}} = MN$. The cost of assigning beam functions is $\mathcal{O}(n_r)$ per beam, where $n_r$ is the number of roots along the beam. Since $n_r$ depends on the object–beam intersection, it depends on the complexity of the objects considered. The complexity of formulating homotopies for the beams is $\mathcal{O}(n_{\text{sec}})$ for linear and non-linear homotopies. In case of spline homotopy, there is an additional one-time cost of inverting a matrix that amounts to a complexity of $\mathcal{O}((4(n_{\text{sec}}-1))^{2.376})$ using the Coppersmith–Winograd algorithm [29]. Such a computational cost can be drastically reduced by formulating a B-spline homotopy where every homotopy de-

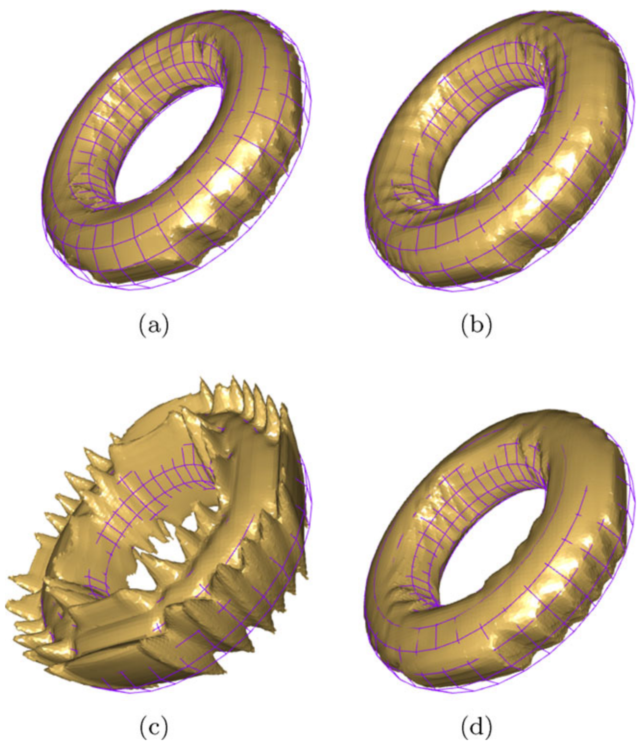


**Fig. 18** Homotopy reconstruction of a torus. (**a**) Linear homotopy. (**b**) Non-linear homotopy with $\eta = 2$. (**c**) Spline homotopy. (**d**) Shape preserving homotopy

pends only on its four neighboring beam functions. Complexity of formulating the monotone homotopy is similar to the linear homotopy once the derivatives are computed (thereby suggesting the local nature). Computation of derivatives is an image space operation and therefore it is $\mathcal{O}(V)$, where $V$ is the number of voxels in the grid of discretized space. Complexity of computing the solution path of the homotopy $\mathbf{H} = 0$ using isosurface extraction is $\mathcal{O}(V)$.

To get a notion of actual computation times for the reconstruction, a scene composed of two primitive objects (a cuboid and a sphere) is reconstructed from its intersection with sonar beams. The computational resource consisted of a 32-processor AMD Quad-Core machine with 256 GB of memory and an OpenMP implementation of the reconstruction algorithm running with 32 threads. Table 6 shows computation times in seconds for all the four reconstruction methods. Here, $T_{bf}$ is the time taken in assigning beam functions to all the sonar beams, $T_{inv}$ is the time taken in inverting the coefficient matrix (in case of cubic homotopy reconstruction), $T_{\mathcal{H}}$ is the time taken in evaluating the homotopy over a grid of volume, and $T_{iso}$ is isosurface computation time. For monotone reconstruction method, $T_{\mathcal{H}}$ includes computation time of derivatives. The reconstruction is computed over a volume grid of size $154 \times 201 \times 201$.

**Table 6** Computation times (in seconds) for reconstruction. The scene composed of a cuboid and a sphere with the reconstruction performed on a raster volume grid of size $154 \times 201 \times 201$.

| | $T_{\mathrm{bf}}$ | $T_{\mathrm{inv}}$ | $T_{\mathcal{H}}$ | $T_{\mathrm{iso}}$ |
|---|---|---|---|---|
| Linear | 0.001328 | | 1.071854 | 1.052210 |
| Non-linear | 0.001322 | | 1.022518 | 1.307745 |
| Cubic | 0.001258 | 0.000247 | 4.100427 | 1.361817 |
| Monotone | 0.001273 | | 3.801818 | 1.169319 |

## 8 Conclusion

We have developed a reconstruction algorithm based on homotopy continuation. Different formulations of homotopies suitable for smooth surface generation were presented. The resulting surface is of good quality both topologically and geometrically. The presented algorithm associates piecewise quadratic functions with the initial and terminal maps. In general, any smooth function that satisfies the design criteria can be used as a beam function. Furthermore, the results are readily extensible to higher dimensions. We conclude that homotopy-based methods are quite powerful in predicting the information from the initial and the terminal maps.

**Acknowledgements** The authors would like to thank collaborators from Simrad Kongsberg Maritime AS and DTU Aqua at the Technical University of Denmark. Special thanks to Lars Nonboe Andersen from Simrad and Bo Lundgren from DTU Aqua for fruitful discussions on Acoustic data processing.

## References

1. Keppel, E.: Approximating complex surfaces by triangulation of contour lines. IBM J. Res. Dev. **19**(1), 2–11 (1975)
2. Fuchs, H., Kedem, Z.M., Uselton, S.P.: Optimal surface reconstruction from planar contours. Commun. ACM **20**(10), 693–702 (1977)
3. Boissonnat, J.D.: Shape reconstruction from planar cross sections. Comput. Vis. Graph. Image Process. **44**(1), 1–29 (1988)
4. Bajaj, C.L., Coyle, E.J., Lin, K.N.: Arbitrary topology shape reconstruction from planar cross sections. Graph. Models Image Process. **58**(6), 524–543 (1996)
5. Boissonnat, J.D., Memari, P.: Shape reconstruction from unorganized cross sections. In: Proceedings of the Fifth Eurographics Symposium on Geometry Processing, p. 98. Eurographics Association (2007)
6. Liu, L., Bajaj, C., Deasy, J.O., Low, D.A., Ju, T.: Surface reconstruction from non-parallel curve networks. In: Computer Graphics Forum, vol. 27, p. 155. (2008)
7. Hoppe, H., DeRose, T., Duchamp, T., McDonald, J., Stuetzle, W.: Surface reconstruction from unorganized points. Comput. Graph. **26**(2), 71–78 (1992)
8. Carr, J.C., Beatson, R.K., Cherrie, J.B., Mitchell, T.J., Fright, W.R., McCallum, B.C., Evans, T.R.: Reconstruction and representation of 3D objects with radial basis functions. In: Proceedings of the 28th Annual Conference on Computer Graphics and Interactive Techniques, pages, p. 76. ACM, New York (2001)

9. Amenta, N., Bern, M.: Surface reconstruction by Voronoi filtering. Discrete Comput. Geom. **22**(4), 481–504 (1999)
10. Zhang, Y., Rohling, R., Pai, D.K.: Direct surface extraction from 3D Freehand ultrasound images. In: IEEE Visualization, pp. 45–52. (2002)
11. Allgower, E.L., Georg, K.: Numerical continuation methods: an introduction. Springer, New York (1990)
12. Shinagawa, Y., Kunii, T.L.: The homotopy model: a generalized model for smooth surface generation from cross-sectional data. Vis. Comput. **7**(2), 72–86 (1991)
13. Berzin, D., Hagiwara, I.: Minimal area for surface reconstruction from cross sections. Vis. Comput. **18**(7), 437–444 (2002)
14. Fujimura, K., Kuo, E.: Shape reconstruction from contours using isotopic deformation. Graph. Models Image Process. **61**(3), 127–147 (1999)
15. Armstrong, M.A.: Basic Topology. Springer, Berlin (1983)
16. Ona, E., Andersen, L.N., Knudsen, H.P., Berg, S.: Calibrating multibeam, wideband sonar with reference targets. In: OCEANS 2007-Europe, pp. 1–5 (2007)
17. Hyman, J.M.: Accurate monotonicity preserving cubic interpolation. SIAM J. Sci. Stat. Comput. **4**(4), 645–654 (1983)
18. Wolberg, G., Alfy, I.: Monotonic cubic spline interpolation. In: Proceedings of Computer Graphics International, 1999, pp. 188–195. (1999)
19. Späth, H.: Exponential spline interpolation. Computing **4**(3), 225–233 (1969)
20. Pruess, S.: An algorithm for computing smoothing splines in tension. Computing **19**(4), 365–373 (1978)
21. Beros, I., Marusic, M.: Evaluation of tension splines. Math Commun **4**, 73–81 (1999)
22. de Boor, C., Swartz, B.: Piecewise monotone interpolation. J. Approx. Theory **21**(4), 411–416 (1977)
23. Costantini, P., Morandi, R.: Monotone and convex cubic spline interpolation. Calcolo **21**(3), 281–294 (1984)
24. Simmonds, E.J., MacLennan, D.N.: Fisheries Acoustics: Theory and Practice. Blackwell, Oxford (2005)
25. Perona, P., Malik, J.: Scale-space and edge detection using anisotropic diffusion. IEEE Trans. Pattern Anal. Mach. Intell. **12**(7), 629–639 (1990)
26. Soille, P.: Morphological Image Analysis: Principles and Applications. Springer, New York (2003)
27. Gonzalez, R.C., Woods, R.E.: Digital Image Processing, 2 edn. Prentice Hall, New York (2002)
28. Aspert, N., Santa-Cruz, D., Ebrahimi, T.: Mesh: Measuring errors between surfaces using the Hausdorff distance. In: Proceedings of the IEEE International Conference on Multimedia and Expo, vol. 1, pp. 705–708. (2002)
29. Coppersmith, D., Winograd, S.: Matrix multiplication via arithmetic progressions. J. Symb. Comput. **9**(3), 251–280 (1990)

**Ojaswa Sharma** has obtained a Ph.D. in Mathematics, Physics, and Informatics from the Technical University of Denmark, Denmark. He received his Bachelor's degree in Civil Engineering from the Indian Institute of Technology at Roorkee, India in 2003. He received his Master's degree in Geomatics Engineering from the University of New Brunswick, Canada in 2006. His research interests include computational geometry, computer graphics, GPU Computing and image processing.

**François Anton** is Associate Professor at the Department of Informatics and Mathematical Modelling of the Technical University of Denmark. He received his Ph.D. in Computer Science from the University of British Columbia (U.B.C., Vancouver, British Columbia, Canada). He has published 1 book, 8 journal papers, 12 book chapters and 50+ conference papers in computing. His interests include computational geometry and topology, computer graphics, interval analysis and databases.